Ocean Engineering 209 (2020) 107513

Contents lists available at ScienceDirect

Ocean Engineering

journal homepage: www.elsevier.com/locate/oceaneng

Variations in directional wave parameters obtained from data measured using a GNSS buoy

Yen-Pin Lin [a], Ching-Jer Huang [b,*], Sheng-Hsueh Chen [c]

[a] Coastal Ocean Monitoring Center (COMC), National Cheng Kung University (NCKU), Tainan, Taiwan
[b] COMC, Department of Hydraulic and Ocean Engineering, NCKU, Tainan, Taiwan
[c] COMC, NCKU, Tainan, Taiwan

ARTICLE INFO

Keywords:
Global navigation satellite system buoy
Displacements and velocities
Signal-to-noise ratio
Mean wave direction
Directional wave spectrum
Dominant wave direction

ABSTRACT

This study investigated variations in directional wave parameters by using various combinations of the GNSS buoy data, such as the displacements ($en\eta$) and the velocities (uvw) in the east, north, and upward directions. The investigated directional wave parameters included mean wave direction, directional spreading, directional wave spectrum, and dominant wave direction (DWD). The three combinations of GNSS buoy data for determining the directional wave parameters were ηuv, $en\eta$, and uvw. Our results revealed that when the significant wave height (H_S) values are $\geq$ 1 m, the signal-to-noise ratios (SNRs) for various measured items are sufficiently large, such that the directional wave parameters obtained from various data, such as $en\eta$, uvw, and ηuv, are identical. By contrast, under smooth to slight sea conditions with an H_S of <1 m, the SNRs for the displacements are small. The small SNRs of $en\eta$ data tend to produce inaccurate directional wave parameters. The deviation in the mean wave direction and DWD obtained from the $en\eta$ data compared with those obtained from the uvw and ηuv data decreases as the H_S increases. For small seas, the uvw and ηuv data are more appropriate than the $en\eta$ data for use in determining directional wave parameters.

1. Introduction

Ocean wave heights, periods, directions, and tide data are essential for coastal engineering and protection projects such as constructing offshore structures like breakwaters (McConnell, 1998) and for determining wave run-up height and overtopping discharge on a seawall (EurOtop, 2018). Directional wave spectra are particularly important for calculating wave loads on offshore structures, forecasting real-time swells, or validating the wave prediction model (Kuik et al., 1988; Goda, 2000).

The directional wave spectra are typically obtained by applying directional analysis methods to wave properties such as elevation, velocity, pressure, and slopes provided by various measuring systems, such as directional buoys, a pressure sensor combined with a two-dimensional (2D) current meter, wave probe arrays, or a remote-sensing system (Benoit and Teisson, 1994).

Benoit (1992) conducted a performance survey of methods used for estimating the directional wave spectra from the heave-pitch-roll data. According to the author's preliminary conclusions, the directional spreading functions (DSFs) around peak frequencies obtained from various methods may differ from one another. The investigated methods included the unimodal Gaussian model, bimodal Mitsuyasu model, Long-Hasselmann method, maximum likelihood method (MLM), iterative MLM, eigenvector method (EVM), iterative EVM, maximum entropy method (MEM), and Bayesian directional method. Benoit (1992) used only the simulated heave-pitch-roll data that were calculated using the unimodal broad spreading function, unimodal thin spreading function, and bimodal spreading function. Benoit and Teisson (1994) further evaluated the capabilities of these methods for determining the directional wave spectra from laboratory wave data obtained from (i) an array of wave probes, (ii) a heave-pitch-roll gauge, and (iii) a wave-velocity gauge.

Young (1994) applied the MLM to determine the DSFs using a spatial array with 4, 5, 6, 7, and 10 water level gauges and noted that the DSFs improved as the number of gauges increased. However, variations in the directional characteristics other than those obtained from the water surface elevations were not investigated.

Riedel and Healey (2005) indicated that by combining time-series

* Corresponding author.
E-mail addresses: lyb57@mail.ncku.edu.tw (Y.-P. Lin), cjhuang@mail.ncku.edu.tw (C.-J. Huang), sean284@mail.ncku.edu.tw (S.-H. Chen).

https://doi.org/10.1016/j.oceaneng.2020.107513
Received 28 March 2019; Received in revised form 27 March 2020; Accepted 9 May 2020
Available online 26 May 2020

data of various parameters, such as displacements and velocities in the east, north, and upward directions, the directional wave spectrum and its spectral parameters could also be determined. Harigae et al. (2005) and Doong et al. (2011) used three-axis displacements and three-axis velocities from a GPS (global positioning system) buoy, respectively, to calculate the directional wave spectra. However, they did not investigate the differences in the directional characteristics by using various combinations of different parameters.

Work (2008) compared the directional energy spectra of nearshore surface waves by analyzing data obtained from a data buoy and an acoustic Doppler current profiler (ADCP). He used the MEM to obtain the directional wave spectra for both systems. For the data buoy, the time-series data of three linear and three angular motions from the data buoy were used. The time-series data of 12 velocities from the ADCP were used: the velocities comprised velocities in the upper three layers, with each layer having four-beam velocities. Work (2008) noted that both systems provided similar mean and peak wave directions. The primary difference was that the directional energy spectra obtained from the ADCP data were more tightly concentrated around the peak direction. This may suggest that either the instrument or the combination of different parameters leads to differences in directional characteristics. However, Work (2008) did not compare the directional characteristics determined from various combinations of parameters.

Panahi et al. (2015) used observed directional wave data from the Nortek Acoustic Wave and Current profiler (AWAC) to calibrate the bimodal DSF by combining DSF models for wind-sea and swell. They determined the best DSF for describing the observed directional wave spectra for a region encountering both wind-sea and swell. A data collection and processing technique used by the AWAC provides directional wave data by combining water surface elevation and horizontal and vertical velocity components (Pedersen and Siegel, 2008).

Although both the wave and tide data are required, the conventional data buoy deployed on the ocean provides only wave data. On the basis of the Virtual Base Station Real Time Kinematics (VBS-RTK) positioning technology, Lin et al. (2017a) and Lin (2018) developed a Global Navigation Satellite System (GNSS) buoy for simultaneously monitoring tides and ocean waves in estuaries and coastal areas. The tide levels obtained from the GNSS buoy were consistent with those from a neighboring tide station. The root-mean-square error of the tide data was within 10 cm. The water surface elevations, significant wave height (H_S) values, zero-crossing periods, 1D wave spectra, directional wave spectra, and dominant wave directions (DWDs or peak wave directions) derived from the GNSS buoy agree very well with those obtained from the accelerometer-tilt-compass (ATC) sensor that is often installed on a data buoy to capture wave data. The GNSS receiver obtained time-series data of six parameters, including longitude, latitude, elevation (hereafter, $en\eta$), and the velocities in the east, north, and upward directions (hereafter, uvw). Lin et al. (2017a) and Lin (2018) used only the water surface elevation and the velocities in the east and north directions (hereafter, ηuv) to obtain the directional wave spectra and directional wave parameters. Please also refer to Sickel (2015) and Kaplan and Hegarty (2017) to obtain more information on the techniques used in GPS and GNSS, ranging from those used in their designs through those used for observation, processing, real-time kinematic (RTK), and real-time networks.

This study investigated the differences in the directional wave parameters obtained using various combinations of the time-series data obtained from the GNSS buoy, such as ηuv, $en\eta$, and uvw. The results may aid practical engineers in selecting appropriate wave properties, such as measured displacements and velocities, to determine directional wave parameters.

2. Methodology

The working principle of the GNSS buoy and GNSS accuracy specifications were reported by Lin et al. (2017a). Lin et al. (2017b) and Lin (2018) examined the performance of the developed GNSS buoy to clarify the effect of the percentage of good elevation data (PGED) on tide and wave monitoring and possible errors in tides and waves that would be caused by the inclination of the buoy hull. Field tests were performed by deploying the buoy in the Wan-Li waters and Small Liu-Qiu waters of Taiwan (Lin et al., 2017b; Lin, 2018). The results from field tests indicated that when the inclination of the buoy hull was not considered, the GNSS tide underestimated a water level by 12 cm as the inclination angle increased up to 16.1°. However, the corrected water levels due to the inclination of the buoy hull did not lead to a significant change in the wave data, such as the H_S, mean wave period, and DWD. The possible reason for the good wave height was that the wave height was obtained from the relative water level data. In the calculation of the wave height, the errors involved in the highest and lowest water levels due to the inclination of the buoy cancel each other out. The inclination of the buoy was accordingly not used to correct the water surface elevations when the wave parameters were determined. The field data used in this study were collected from 00:00 October 15 to 23:00 October 30, 2016, from the Small Liu-Qiu data buoy. The GNSS buoy measured the ellipsoidal height, horizontal positions, velocities, and quality index hourly. The sampling rate was 1 Hz. The data acquisition system was turned on at the 48th minute of each hour to warm up the system for 2 min, and it began to acquire samples at the 50th minute. The data were thus collected for 10 min. Therefore, in each hour, 600 monitoring data were collected for each measuring item. The monitored data were transmitted via the GPRS modem to the receiving system for further data processing. The outlook and location of the Small Liu-Qiu buoy are presented in Figs. 1 and 2, respectively. For the details of the deployment of the Small Liu-Qiu buoy, please refer to Lin (2018). In the current study, the water surface elevation is denoted by η; displacements in the east and north directions by e and n, respectively; and velocities in the east, north, and upward directions by u, v, and w, respectively.

2.1. Calculating positions and velocities using a GNSS

Lin et al. (2017a) and Lin (2018) have discussed the VBS-RTK positioning technology used to determine the position of a buoy. The VBS-RTK system used in our work consisted of three components, namely a GNSS base station network, a control center, and a rover station. Their respective functions were as follows:

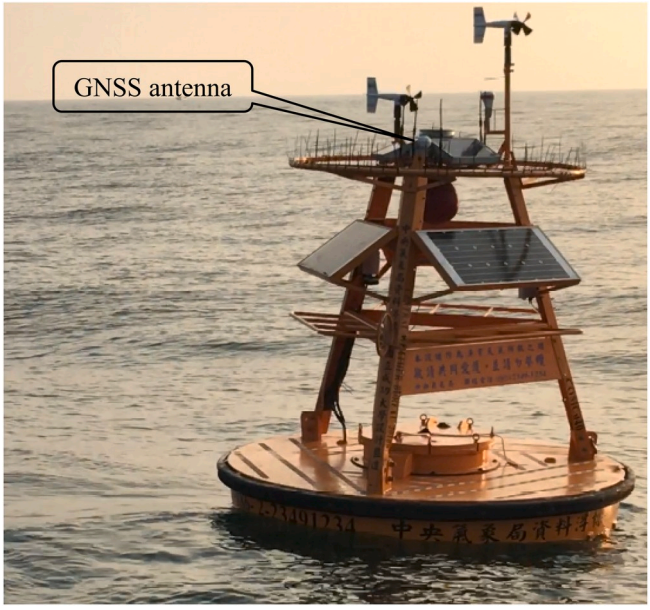

Fig. 1. Outlook of the Small Liu-Qiu buoy.

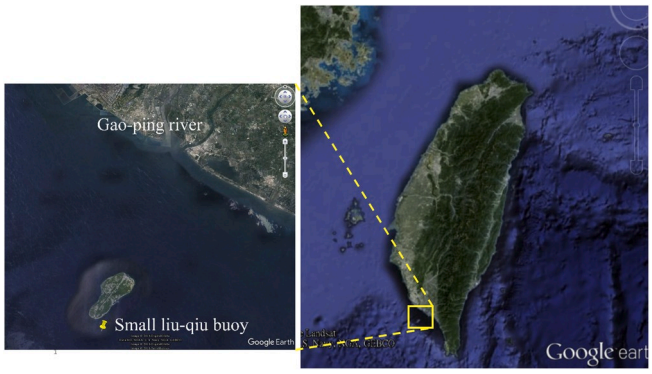

Fig. 2. Location of the Small Liu-Qiu buoy.

1. GNSS base station network: Each base station received GNSS observation data and transmitted the raw data to the control center continuously. Currently, 78 base stations were implemented in Taiwan.
2. Control center: The VBS-RTK control center for positioning computation used in this work was operated by the National Land Surveying and Mapping Center (NLSC) of the Ministry of the Interior, Taiwan. It supported both GPS and GLONASS constellations. The Progressive Infrastructure Via Overlaid Technology (PIVOT) commercial software program developed by Trimble Navigation was run in the center.
3. Rover station: The rover station consisted of a GNSS buoy with a GNSS receiver and a GNSS antenna attached to it.

The procedure of VBS positioning was conducted as follows:

1. Pre-process network observations: Establishing the network database and completing the coordinate adjustments for each base station.
2. Obtaining data from regional stations: Collecting continuous observations and accurate coordinates from each GNSS base station, thus establishing an area correction parameters database.
3. Generating VBS data for the rover: The rover station reported approximate coordinates to the VBS-RTK control center. According to the carrier phase observations, the PIVOT software program continuously calculated the errors caused by the multipath, ionosphere, troposphere, and ephemeris and the integer ambiguity of the carrier phase of L1 and L2. It also established a VBS dataset at a location near the rover station. Subsequently, the VBS data were transmitted to the rover station.
4. Calculating the position of the rover station: The rover station received the VBS data and processed to ultra-short-baseline RTK positioning.

Wu et al. (2013) provided detailed information on the precision of positions obtained using the VBS-RTK system operated by the NLSC. They reported that the total accuracies of positions for the GPS satellite positioning reference network and VBS-RTK were approximately 2 cm and 5 cm in the horizontal and vertical directions, respectively.

The GNSS receiver estimated the velocities using the Doppler shift with an accuracy in the order of some cm/s. According to He (2015), the fundamental principle for determining velocities is equation of Doppler shift for the satellite S and the GNSS receiver R as written in Eq. (1).

$$D^S_{R,j} = \frac{V_r}{c} f^S_j \tag{1}$$

where $D^S_{R,j}$ is the shift in frequency between the satellite S and the receiver R at the $j-th$ frequency channel, f denotes the frequency of the GNSS carrier phase observation, V_r is the radial velocity of the satellite S relative to the receiver R, and c denotes the speed of light in a vacuum. $D^S_{R,j}$ had a positive sign when the receiver and the transmitter approached each other and a negative sign when the receiver and the transmitter moved away from each other. The GNSS receiver used in this study could receive carrier phase signals from the satellites. According to its specification (Topcon Positioning Systems, 2012), the accuracy of the velocity was 0.02 m/s circular error probability, which was 1.2 times the root-mean-square accuracy of the velocity.

The procedure for using a GNSS buoy, based on VBS-RTK positioning, to calculate positions and velocities can be summarized as follows:

1. A GNSS receiver on the buoy receives signals from satellites and uses these data to calculate its velocity and approximate position (longitude, latitude, and elevation).
2. The position and GPS time data are transmitted to the VBS-RTK control center through a general packet radio service (GPRS) modem.
3. The VBS-RTK control center generates VBS data by using the PIVOT software and then transmits the data back through the GPRS modem to the GNSS receiver on the buoy.
4. The GNSS receiver determines the corrected position and the quality index on the basis of the received satellite signals and VBS data. These data are then transmitted to the receiving system on land.

2.2. PGED (percentage of good elevation data)

According to some key factors, including the signals received by the GNSS buoy and GNSS base station network, the network signal quality of the GNSS buoy and GNSS base station network, and ionospheric activity, the GNSS buoy obtains specific resolution results with specific quality indicators. When the quality indicator shows "4 – RTK Fix solution," the instantaneous resolution result is identified as good elevation data (GED). Thus, the hourly PGED is determined as the ratio of the number of GED to the number of observed data (i.e., 512), and defined as follows.

$$\mathrm{PGED} = \frac{\mathrm{GED}}{512} \tag{2}$$

Based on the adopted sampling rate 1 Hz and the sampling period 10 min/h, 600 data are available for further data analyzing. Only the first 512 data are used. In this study, only hourly data, with PGED = 1.00, are used to determine the directional wave parameters, such as the mean wave direction, directional spreading, directional wave spectrum, and DWD.

2.3. Directional wave spectra determined from ηuv data

Hashimoto and Konbune (1988) described the relationship between the directional wave spectrum and the cross-power spectrum for any pair of wave properties, such as η, u, and v, as follows:

$$\Phi_{\mathrm{mn}}(f) = \int_{-\pi}^{\pi} I_m(f,\theta) I_n^*(f,\theta)\{\cos[k(x_{mn}\cos\theta + y_{mn}\sin\theta)] - \\ - i\sin[k(x_{mn}\cos\theta + y_{mn}\sin\theta)]\} S(f,\theta)\, d\theta \tag{3}$$

where f is the frequency, θ is the wave propagation angle measured from the x-axis (east direction) and increased in the counterclockwise direction, $\Phi_{mn}(f)$ is the cross-power spectrum between the m-th and n-th wave properties, $I_m(f,\theta)$ is the transfer function from the water surface elevation to the m-th wave property, the asterisk (*) denotes the conjugate complex, k is the wavenumber, $x_{mn} = x_n - x_m$, $y_{mn} = y_n - y_m$, (x_m, y_m) is the location of the wave probe for the m-th wave property, i is the imaginary unit, and $S(f,\theta)$ is the directional wave spectrum.

When the ηuν data are used, the vertical elevation (η) and the ve-

locities in the east and north directions (u and v, respectively) are measured by the same GNSS antenna. Accordingly, $x_{mn} = 0$ and $y_{mn} = 0$, and Eq. (3) can be simplified as follows:

$$\Phi_{\mathrm{mn}}(f) = \int_{-\pi}^{\pi} I_m(f,\theta) I_n^*(f,\theta)\, S(f,\theta)\, d\theta \tag{4}$$

with

$$\mathrm{I}_m(f,\ \theta) = h_m(f)\cos^{\alpha}\theta\, \sin^{\beta}\theta \tag{5}$$

where the function h_m and the parameters α and β vary with the wave properties and were provided by Hashimoto and Konbune (1988). When Eq. (5) is substituted into Eq. (4), the cross-power spectra between the various wave properties can be obtained.

The directional wave spectrum, $\mathrm{S}(f,\theta)$, could be determined as follows:

$$\mathrm{S}(f,\theta) = \mathrm{D}(f,\theta)\mathrm{C}_{\eta\eta}(f) \tag{6}$$

$$\mathrm{D}(f,\theta) = \frac{1}{\pi}\{\frac{1}{2} + \sum_{n=1}^{2}[a_n^{'}(f)\cos n\theta + b_n^{'}(f)\sin n\theta]\} \tag{7}$$

where $\mathrm{D}(f,\theta)$ is the directional spreading function, $\mathrm{C}_{\eta\eta}(f)$ is the 1D wave spectrum, $a_n^{'}(f)$ and $b_n^{'}(f)$ are the Fourier coefficients, and n is the order of the Fourier series. Lin et al. (2017a) provided the equations for determining the Fourier coefficients of $\mathrm{D}(f,\theta)$ from the ηuv data. These equations are given as follows:

$$a_1^{'}(f) = \frac{C_{\eta u}(f)}{\sqrt{C_{\eta\eta}(f)[C_{uu}(f) + C_{vv}(f)]}} \tag{8}$$

$$b_1^{'}(f) = \frac{C_{\eta v}(f)}{\sqrt{C_{\eta\eta}(f)[C_{uu}(f) + C_{vv}(f)]}} \tag{9}$$

$$a_2^{'}(f) = \frac{C_{uu}(f) - C_{vv}(f)}{C_{uu}(f) + C_{vv}(f)} \tag{10}$$

$$b_2^{'}(f) = \frac{2C_{uv}(f)}{C_{uu}(f) + C_{vv}(f)} \tag{11}$$

where $C_{mn}(f)$ is the cospectrum between the m-th and n-th wave properties. The cospectrum is the real part of the complex cross-power spectrum. Note also that the cross-power spectrum of two identical wave properties has no imaginary part; therefore, it was identical to the cospectrum of these two wave properties, namely

$$\Phi_{mm}(f) = C_{mm}(f) \tag{12}$$

2.4. Directional wave spectra obtained from enη data

Riedel and Healey (2005) indicated that by using the $en\eta$ data, the Fourier coefficients of $\mathrm{D}(f,\theta)$ could be determined as follows:

$$a_1^{'}(f) = \frac{\mathrm{Im}\,[\Phi_{e\eta}(f)]}{\sqrt{\Phi_{\eta\eta}(f)[\Phi_{ee}(f) + \Phi_{nn}(f)]}} \tag{13}$$

$$b_1^{'}(f) = \frac{\mathrm{Im}\,[\Phi_{n\eta}(f)]}{\sqrt{\Phi_{\eta\eta}(f)[\Phi_{ee}(f) + \Phi_{nn}(f)]}} \tag{14}$$

$$a_2^{'}(f) = \frac{\Phi_{ee}(f) - \Phi_{nn}(f)}{\Phi_{ee}(f) + \Phi_{nn}(f)} \tag{15}$$

$$b_2^{'}(f) = \frac{2\mathrm{Re}[\Phi_{en}(f)]}{\Phi_{ee}(f) + \Phi_{nn}(f)} \tag{16}$$

where Im and Re denote the imaginary and real parts of the cross-power spectrum, respectively. Riedel and Healey (2005) also indicated that these coefficients had been incorporated in the Datawell Directional Waverider to determine the directional wave spectrum. The 3D displacements are obtained by integrating the 3D accelerations measured by the buoy. In this study, the 3D displacements were measured directly by the GNSS buoy.

As mentioned earlier, the cross-power spectrum of two identical wave properties has no imaginary part. Based on Eq. (12), Eqs. (13)–(16) can be rewritten as follows.

$$a_1^{'}(f) = \frac{\mathrm{Im}\,[\Phi_{e\eta}(f)]}{\sqrt{\mathrm{C}_{\eta\eta}(f)[\mathrm{C}_{ee}(f) + \mathrm{C}_{nn}(f)]}} \tag{17}$$

$$b_1^{'}(f) = \frac{\mathrm{Im}\,[\Phi_{n\eta}(f)]}{\sqrt{\mathrm{C}_{\eta\eta}(f)[\mathrm{C}_{ee}(f) + \mathrm{C}_{nn}(f)]}} \tag{18}$$

$$a_2^{'}(f) = \frac{\mathrm{C}_{ee}(f) - \mathrm{C}_{nn}(f)}{\mathrm{C}_{ee}(f) + \mathrm{C}_{nn}(f)} \tag{19}$$

$$b_2^{'}(f) = \frac{2\mathrm{Re}[\Phi_{en}(f)]}{\mathrm{C}_{ee}(f) + \mathrm{C}_{nn}(f)} \tag{20}$$

2.5. Directional wave spectra obtained from uvw data

Riedel and Healey (2005) also provided equations for determining the Fourier coefficients of $\mathrm{D}(f,\theta)$ from the uvw data measured by a tri-directional current meter. Their equations were modified as follows.

$$a_1^{'}(f) = \frac{\mathrm{Im}\,[\Phi_{wu}(f)]}{\sqrt{C_{ww}(f)[C_{uu}(f) + C_{vv}(f)]}} \tag{21}$$

$$b_1^{'}(f) = \frac{\mathrm{Im}\,[\Phi_{wv}(f)]}{\sqrt{C_{ww}(f)[C_{uu}(f) + C_{vv}(f)]}} \tag{22}$$

$$a_2^{'}(f) = \frac{C_{uu}(f) - C_{vv}(f)}{C_{uu}(f) + C_{vv}(f)} \tag{23}$$

$$b_2^{'}(f) = \frac{2\mathrm{Re}[\Phi_{uv}(f)]}{C_{uu}(f) + C_{vv}(f)} \tag{24}$$

In this study, the displacement and velocity are measured by the GNSS buoy, Fast Fourier Transform (FFT) was applied to determine the cospectrum (the real part of cross-power spectrum) and the quadrature spectrum (the imaginary part of the cross-power spectrum) for any pair of wave properties, such as u, v, and w. The obtained cross-power spectra were then used to determine the Fourier coefficients of the directional spreading function $D(f,\theta)$, such as Eqs. (8)–(11) for the ηuv data, Eqs. (17)–(20) for the $en\eta$ data, and Eqs. (21)–(24) for the uvw data.

2.6. Weighted Fourier series method

Longuet-Higgins et al. (1963) calculated the directional spectrum of ocean waves by using the floating buoy motions, including the water surface elevations and slopes in the east and north directions. The authors indicated that the DSF might be negative and therefore proposed the weighting coefficients to correct the DSF. The weighted Fourier coefficients were expressed as follows:

$$a_1^{''}(f) = \frac{2}{3}a_1^{'}(f) \tag{25}$$

$$b_1^{''}(f) = \frac{2}{3}b_1^{'}(f) \tag{26}$$

$$a_2^{''}(f) = \frac{1}{6}a_2^{'}(f) \tag{27}$$

$$b_2^{''}(f) = \frac{1}{6}b_2^{'}(f) \tag{28}$$

Here, we adopt above-weighted Fourier coefficients to determine the directional spreading functions by using the *ηuv*, *enη*, and *uvw* data measured by the GNSS buoy. Accordingly, Eq. (7) can be rewritten as follows:

$$D(f,\theta)=\frac{1}{\pi}\{\frac{1}{2}+\sum_{n=1}^{2}[a_n^{''}(f)\cos n\theta+b_n^{''}(f)\sin n\theta]\} \quad (29)$$

Longuet-Higgins et al. (1963) also indicated that the weighted Fourier coefficients would extend the width of the DSF. Accordingly, the values of the DSF thus obtained would be larger than those obtained using non-weighted Fourier coefficients.

2.7. Mean wave direction and directional spreading

To determine the directional characteristics of ocean waves, two parameters were also often used, namely the mean wave direction and directional spreading. The mean wave direction represents the average propagation direction of ocean waves, whereas the directional spreading is a measure of the directional spreading of wave energy. According to Kuik et al. (1988), the mean wave direction $\theta_m(f)$ and the directional spreading $\sigma_\theta(f)$ could be expressed in terms of the first-order Fourier coefficients as follows:

$$\theta_m(f)=\tan^{-1}\frac{b_1^{''}(f)}{a_1^{''}(f)} \quad (30)$$

$$\sigma_\theta(f)=\sqrt{2\,[1-(a_1^{''}(f)\cos\theta_m(f)+b_1^{''}(f)\sin\theta_m(f))]} \quad (31)$$

Notably, both the mean wave direction and directional spreading are functions of the frequency. However, here, the mean wave direction and directional spreading denote their values at the peak frequency. The peak frequency denotes the frequency of waves with the maximum power spectral density in the 1D wave spectrum.

3. Results and discussion

This study applied the weighted Fourier series (WFS) method proposed by Longuet-Higgins et al. (1963) to investigate variations in directional wave parameters by using the *ηuv*, *enη*, and *uvw* data obtained from the GNSS buoy deployed in the Small Liu-Qiu waters, Taiwan. The outlook and location of the Small Liu-Qiu buoy are shown in Figs. 1 and 2, respectively. The investigated directional wave parameters included the mean wave direction, directional spreading, directional wave spectrum, and DWD. The field data were collected in 2016 from 10/15/00:00 (this notation refers to month/day/hour, hereafter) to 10/30/23:00. However, only hourly data, with PGED = 1.0, were used to determine the wave parameters.

3.1. Sea states during the field test period of GNSS buoy

To provide more information to understand the temporal variations in directional wave parameters, the significant wave heights (H_S) in the Small Liu-Qiu waters during the field test period were analyzed (Fig. 3). Fig. 3 displays the hourly time-series data of the significant wave height obtained using the GNSS buoy and ATC sensor data. The ATC sensor was installed on the buoy to provide additional wave data to be compared with those obtained from the GNSS receiver. The ATC sensor measurements were conducted on an hourly basis. Each measurement was conducted for a duration of 10 min and at a sampling rate of 1 Hz. Lin et al. (2017a) listed the detailed specifications of the ATC sensor used in this study. The significant wave height was calculated from the one-dimensional (1D) wave spectrum as follows:

$$H_S=4\sqrt{m_0} \quad (32)$$

$$m_0=\int_0^\infty s(f)df \quad (33)$$

where m_0 denotes the zero-th moment of the 1D wave spectrum, and $s(f)$ is the spectral density at frequency f. H_S values obtained from the ATC sensor were calculated from the power spectral density of water surface elevation (η) based on the method proposed by Earle (1996). For a GNSS buoy, $s(f)$, which equals $C_{\eta\eta}(f)$, was calculated after the water surface elevations were obtained, and the H_S values were then determined using Eqs. (32) and (33). Because only hourly GNSS data with a PGED value of 1.0 were used to determine the wave data, no H_S values were obtained from the GNSS buoy for some hours. Fig. 3 reveals that the H_S values obtained from the GNSS buoy are mostly in close agreement with those obtained from the ATC sensor. Furthermore, a detailed analysis of 159 H_S data samples obtained from both the GNSS buoy and ATC sensor

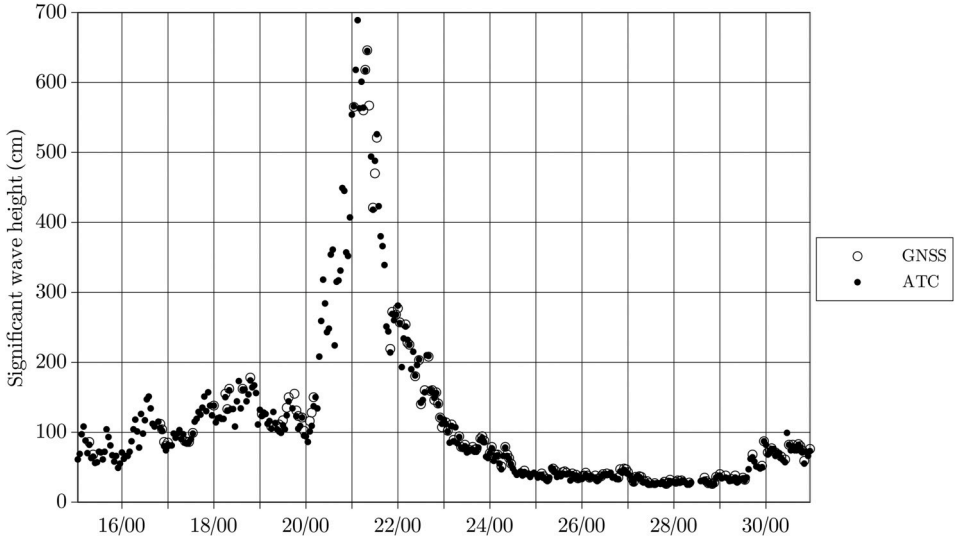

Fig. 3. Hourly time-series data of the significant wave height H_S obtained from the GNSS buoy and ATC sensor. The digits on the abscissa indicate the day and hour in October 2016. The field data were collected from 00:00 on October 15 to 23:00 on October 30 in 2016. Because only GNSS data with a PGED value of 1.0 were analyzed, no H_S data were obtained from the GNSS buoy for some hours.

revealed that the mean absolute error between the two data sets was 2.9 cm.

Fig. 3 reveals that the missing H_S values from the GNSS buoy data mainly corresponded to the hours with heavy winds and waves. The GPRS connection dropout during severe weather conditions may restrict the number of GED and make the hourly PGED value less than 1.0; consequently, no H_S values would be obtained from the GNSS buoy. This situation poses a serious operational problem when the GNSS buoy based on VBS-RTK positioning is used for ocean monitoring.

A typhoon occurred near Taiwan during the field test period. Thus, large wave heights were measured. Fig. 4 illustrates the track of Typhoon Haima, and Fig. 3 reveals that the H_S values exceeded 2.0 m from 10/20/06:00 to 10/22/11:00 and exceeded 4.0 m from 10/20/23:00 to 10/21/11:00 because Typhoon Haima was then closest to Taiwan. By contrast, during the period from 10/24/11:00 to 10/29/11:00, 2016, the Small Liu-Qiu waters were smooth with H_S values less than 0.4 m. In this study, the words used to describe the sea states match the WMO (World Meteorological Organization) terminology for sea states.

3.2. Mean wave direction

Fig. 5 (a) displays the hourly time-series data of mean wave direction and their differences obtained using the ηuv and $en\eta$ data. The angles were measured clockwise from the north. Fig. 5 (b) presents the corresponding results obtained using the uvw and ηuv data. Fig. 5 (b) reveals that the differences in the mean wave direction obtained using the uvw and ηuv data ranged between -8° and 11° for diverse wave heights. Fig. 5 (a) shows that from 10/17/11:00 to 10/23/06:00 the differences in the mean wave directions obtained from the $en\eta$ and ηuv data are quite small and become large from 10/23/06:00 to 10/30/23:00. Comparing to Fig. 3, it can be noted that the former period corresponds to moderate and higher sea conditions with $H_S \geq 1.0\,m$, whereas the latter period corresponds to smooth to slight sea conditions with $H_S < 1.0\,m$. The maximum angular difference in the mean wave direction obtained using $en\eta$ and ηuv data was 156^o (or 204^o when the angles were measured clockwise), and it occurred at 10/26/00:00, 2016. At this time, the measured H_S was as low as 0.37 m, indicating a smooth sea state, and the obtained mean wave directions were 138^o, 342^o, and 146^o by using the ηuv, $en\eta$, and uvw data, respectively. The mean wave direction determined from the $en\eta$ data was close to that determined using two other data sets, except under calm sea states. The reasons for this difference are discussed in Sections 3.4 and 3.6.

3.3. Directional spreading

The hourly time-series data of directional spreading and their differences obtained from the ηuv and $en\eta$ data are displayed in Fig. 6 (a), whereas the corresponding results obtained from the uvw and ηuv data are presented in Fig. 6 (b). Comparing Fig. 6 (a) and 6 (b) reveals that from 10/17/11:00 to 10/23/06:00 the differences in directional spreading obtained from the ηuv and $en\eta$ data were close to those obtained from the ηuv and uvw data. However, the differences become larger from 10/23/06:00 to 10/30/23:00. The former period corresponds to sea states with $H_S \geq 1.0\,m$, whereas the latter period corresponds to sea states with $H_S < 1.0\,m$. Fig. 6 (b) reveals that the directional spreading values obtained using the uvw and ηuv data differ slightly for diverse wave heights, except that occurred at 10/21/13:00, 2016. The angular difference was -9^o.

3.4. Directional wave spectrum

Directional wave spectra calculated using the $en\eta$ and ηuv data, collected from 10/25/21:00 to 10/26/02:00/26/10, are shown in the

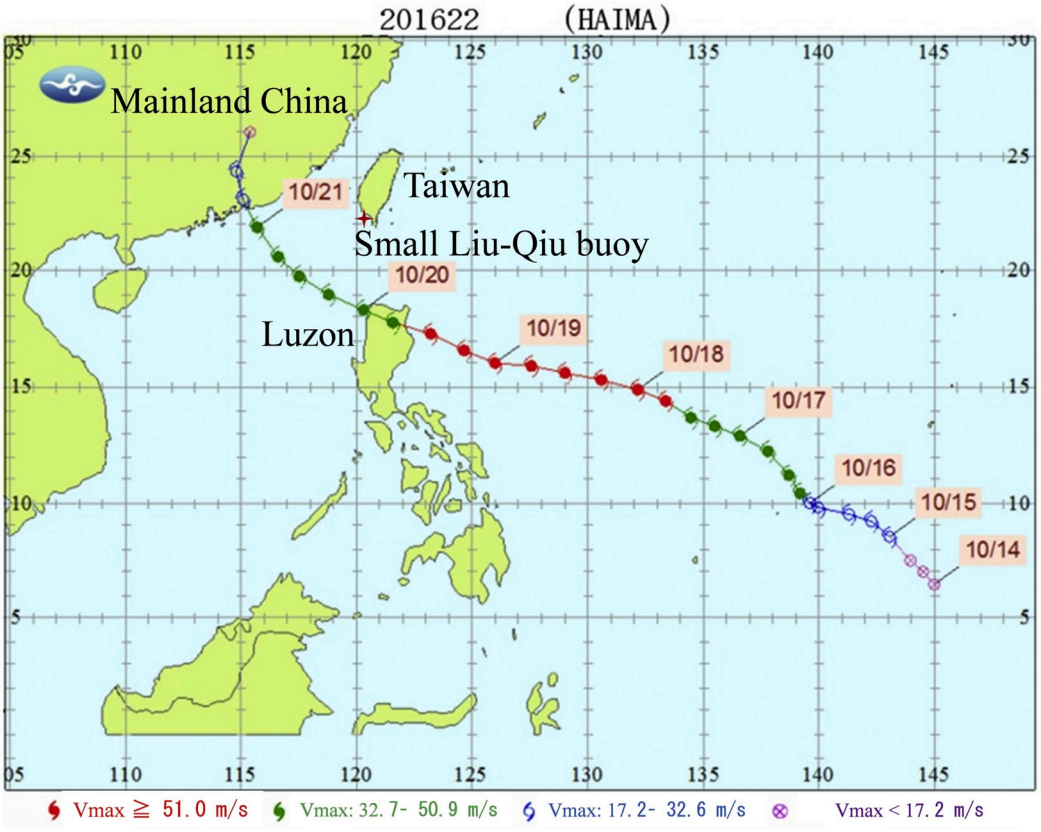

Fig. 4. Path of typhoon Haima.

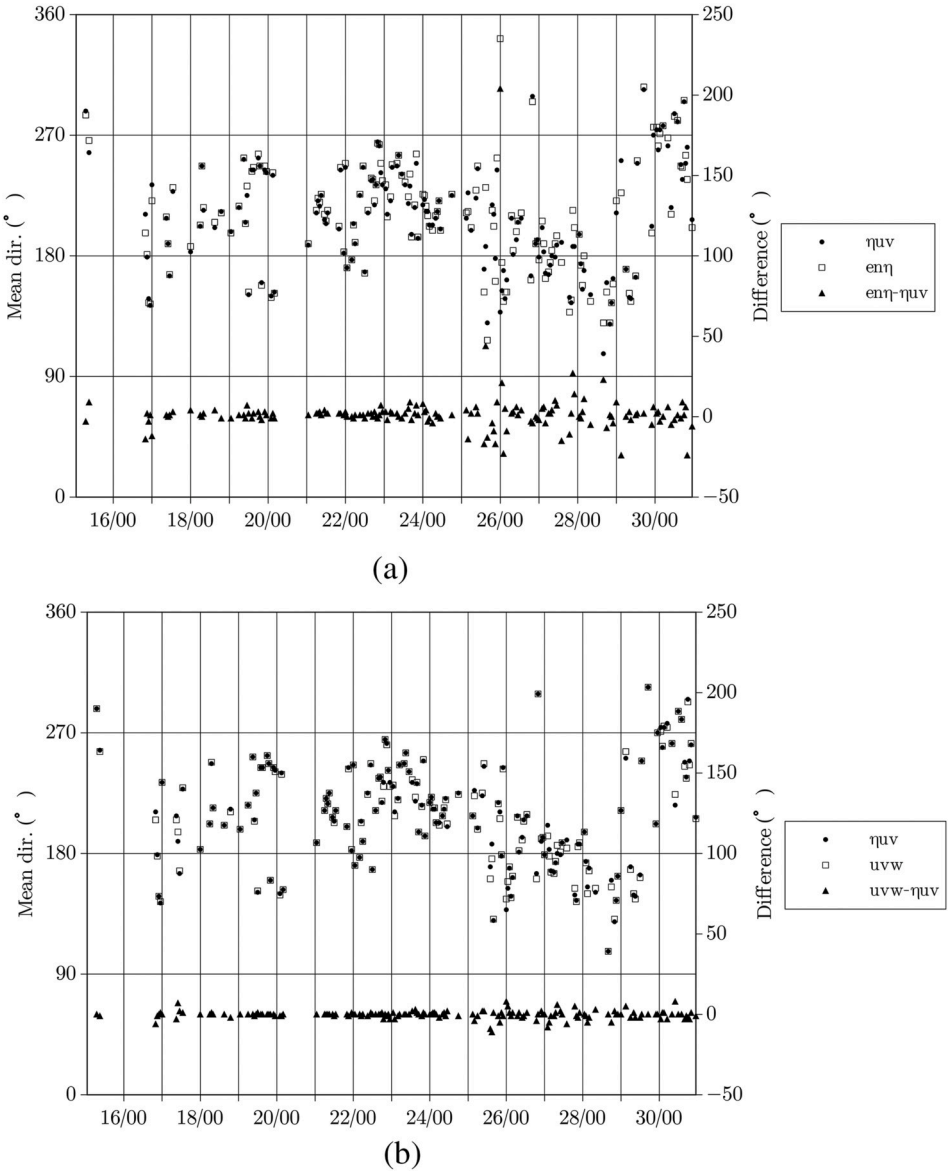

Fig. 5. Hourly time-series data of mean wave direction and their differences obtained using (a) the *ηuv* and *enη* data and (b) the *ηuv* and *uvw* data, measured by the Small Liu-Qiu buoy. The field data were collected from 00:00 on October 15 to 23:00 on October 30 in 2016, but only hourly data with PGED = 1.0 were analyzed. The digits on the abscissa indicate the day and hour in October.

left and right sides of Fig. 7, respectively. During this period, the H_S values were <1 m. The azimuth of the circular plot illustrates the direction from which ocean waves came. The angles 0°, 90°, 180°, and 270°indicate the north, east, south, and west directions, respectively. The radial direction indicates the wave frequency in hertz. Furthermore, the peak frequency and the DWD are also shown in the upper-left corner of each figure. The DWD is identified as the direction where the maximum power spectral density (unit: m^2/Hz/rad) occurs. The color bar indicates the strength of the power spectral density.

Notably from Fig. 7 that the directional wave spectra determined using the *enη* data are similar to those determined using the *ηuv* data, except those obtained at 10/26/00:00. During the observation period, as depicted in Fig. 7, the ocean wave mainly originated from the south semicircle except for that determined using the *enη* data at 10/26/00:00. Comparison with the ATC data (see Section 3.6) indicates that the *enη* results are likely wrong. Furthermore, at this particular time, the peak wave energy obtained from the *enη* data originated from the NW direction, despite the wind originating from the south. Thus, the directional wave spectrum obtained at 10/26/00:00 by using the *enη* data is unreasonable. The possible reasons that caused this inaccuracy are discussed in Section 3.6.

Fig. 3 shows that from 10/18/00:00 to 10/23/04:00, the H_S values in the Small Liu-Qiu waters were larger than 1 m. Fig. 8 compares some of the directional wave spectra determined by using the *ηuv*, *enη*, and *uvw* data from 06:00 to 11:00 on October 21, 2016. During this period, the Typhoon Haima was close to Taiwan; hence, the H_S exceeded 6.0 m. Notably, as shown in Fig. 8, the directional wave spectra obtained from the *ηuv*, *enη*, and *uvw* data were mainly identical. Furthermore, all the waves with peak energy were from the southwest direction and the peak frequencies were very low (0.0859 Hz or 0.0957 Hz), probably because of the typhoon-induced swell. Notably from Figs. 2 and 4 that the typhoon Haima was in the west-southwest direction of the Small Liu-Qiu

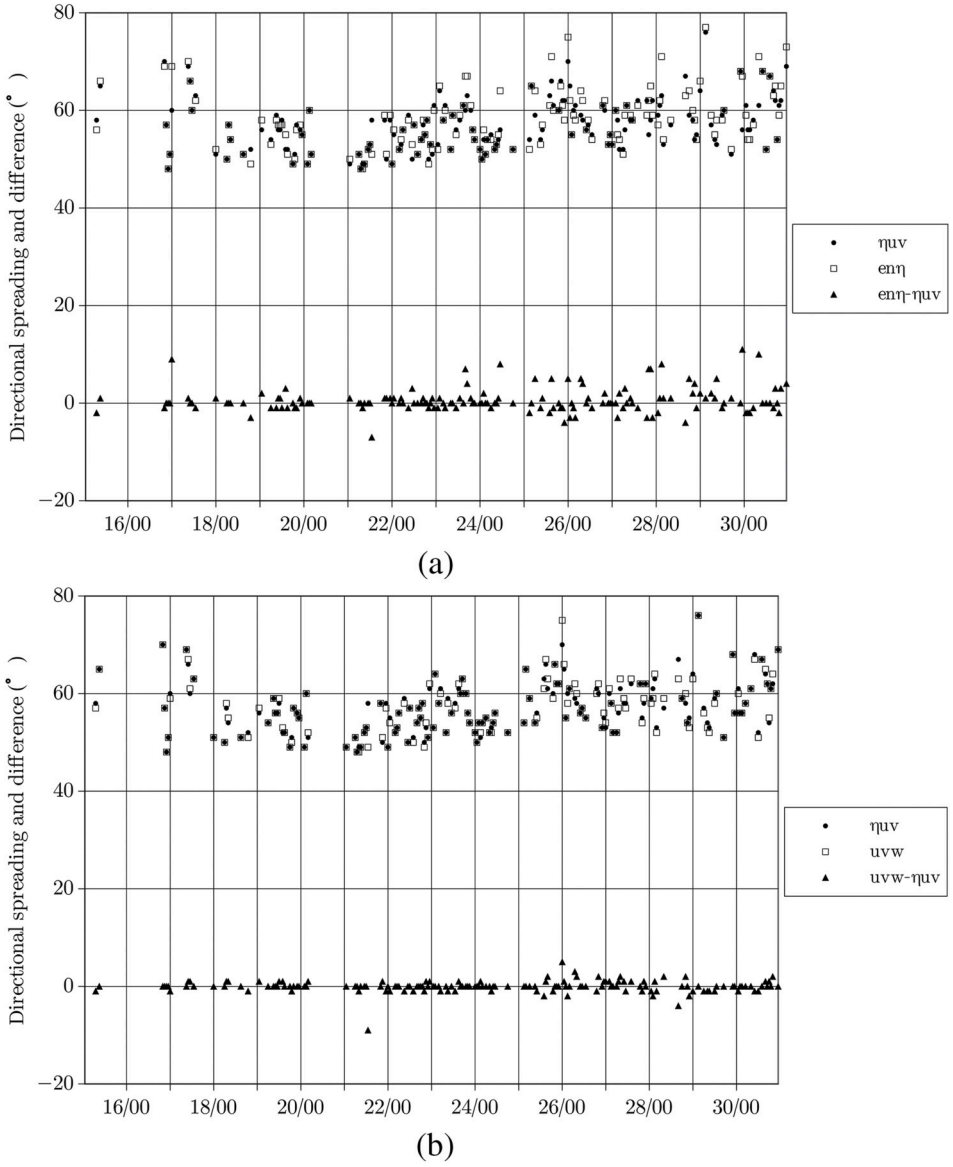

Fig. 6. Hourly time-series data of directional spreading and their differences obtained using (a) the *ηuv* and *enη* data and (b) the *ηuv* and *uvw* data, measured by the Small Liu-Qiu buoy. The field data were collected from 00:00 on October 15 to 23:00 on October 30 in 2016, but only hourly data with PGED = 1.0 were analyzed. The digits on the abscissa indicate the day and hour in October.

buoy on October 21, 2016. The results shown in Figs. 7 and 8 reveal that at small seas, the directional wave spectra obtained from the *enη* data differ from those obtained using the *ηuv* data; however, at high seas, the directional wave spectra obtained using three data combinations were identical.

3.5. DWD (dominant wave direction)

Fig. 9 (a) shows the hourly time-series of the DWD and their differences determined using the *ηuv* and *enη* data collected by the GNSS buoy from 10/15/00:00 to 10/30/23:00, 2016; whereas Fig. 9 (b) displays the corresponding results obtained using the *uvw* and *ηuv* data. The DWD is the direction from which an ocean wave with peak energy comes, and the angle is measured clockwise from the north. Notably from Fig. 9 that the differences in the DWD obtained using the *uvw* and *ηuv* data were primarily in the $\pm 1.25^o$ range (90.7%), whereas those obtained using the *enη* and *ηuv* data were primarily in the $\pm 30^o$ range (93.2%), indicating that the DWDs obtained using the *uvw* and *ηuv* combinations of GNSS buoy data were mostly identical. However, as shown in Fig. 9 (a), we noted that the maximum difference in the DWD between the *enη* and *ηuv* data was 169^o, which occurred at 10/26/00:00 and was the same as the time when the maximum difference in the mean wave direction obtained using the *enη* and *ηuv* data occurred. The dominant wave direction determined from the *enη* data was apparently different from those determined using two other data sets. Reasons for this difference are discussed in Section 3.6.

Both the mean wave direction and DWD are widely adopted to indicate the wave directions. As mentioned, the mean wave direction represents the average propagation direction of ocean waves; whereas the DWD denotes the wave direction where the maximum power spectral density occurred in the 2D wave spectrum; the difference between them could be noteworthy. The histogram of the differences between the

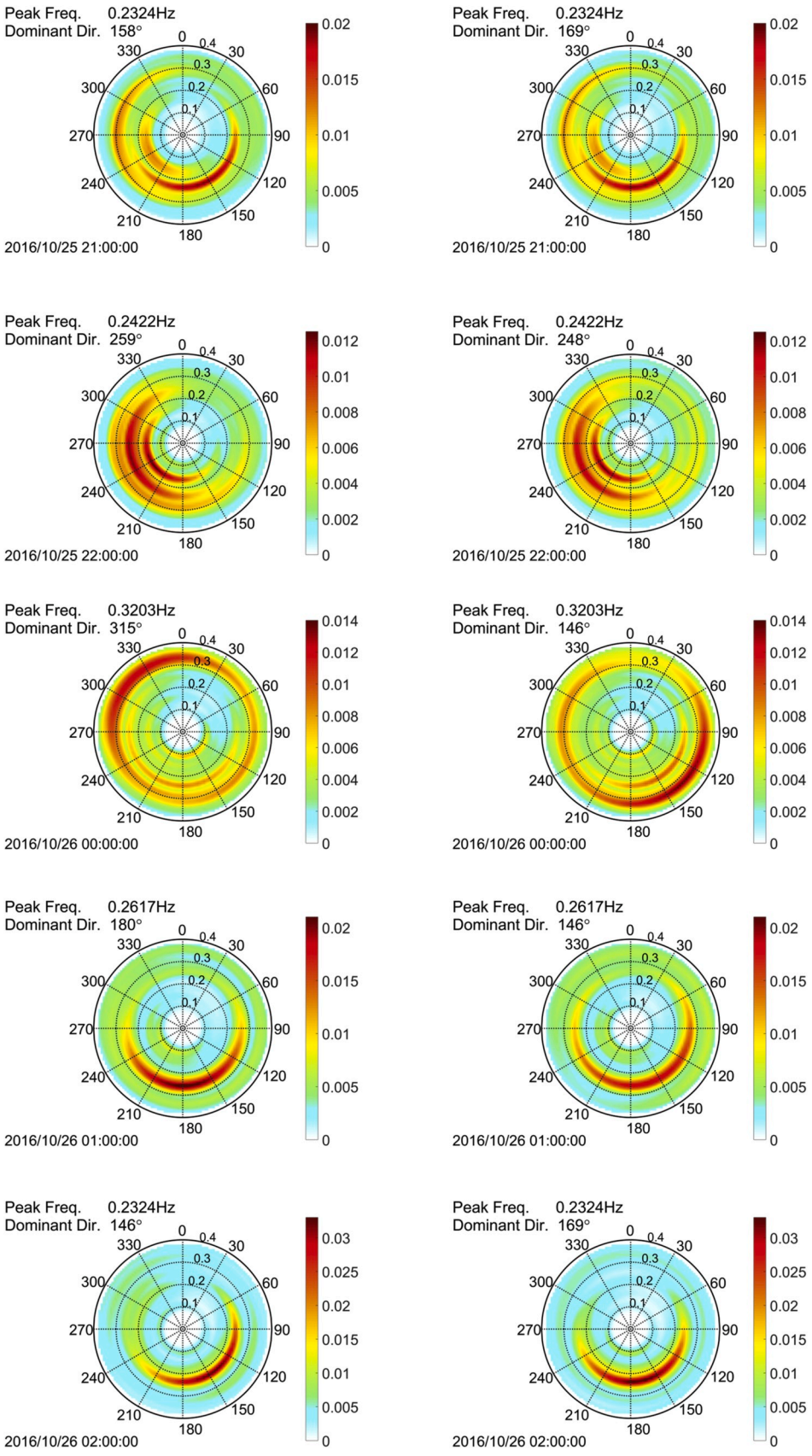

Fig. 7. Directional wave spectra obtained using the *enη* (left) and *ηuv* (right) data collected from 21:00 on October 25 to 02:00 on October 26, 2016; during this period the H_S values were <1 m, indicating smooth to slight sea conditions. The color bar indicates the strength of the power spectral density (unit: m^2/Hz/rad). (For interpretation of the references to color in this figure legend, the reader is referred to the Web version of this article.)

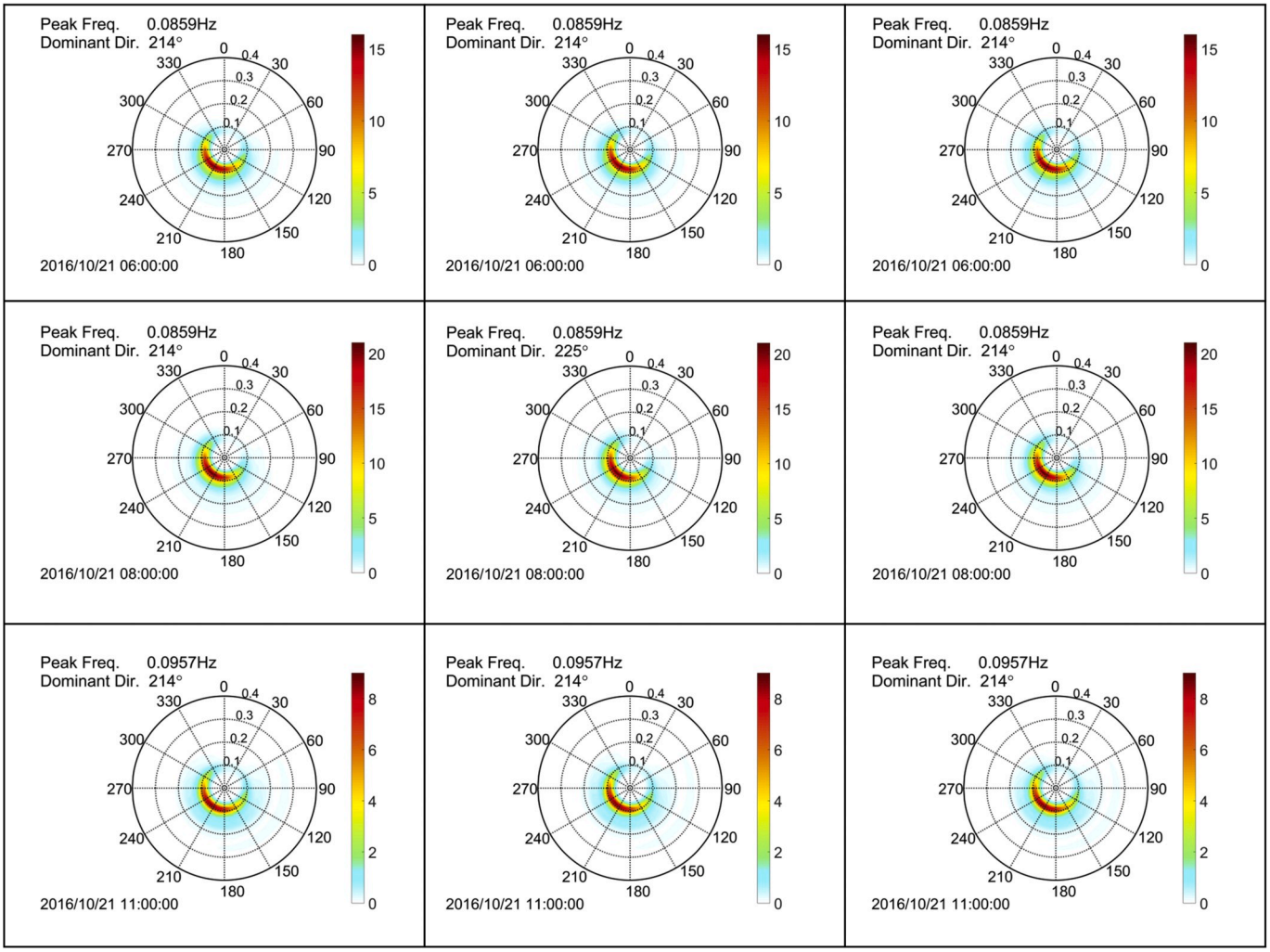

Fig. 8. Directional wave spectra obtained using the ηuv (left), $en\eta$ (middle), and uvw (right) data at 06:00, 08:00, and 11:00 on October 21, 2016, respectively; during this period, because of Typhoon Haima, the H_S values exceeded 6.0 m. The color bar indicates the strength of the power spectral density. (For interpretation of the references to color in this figure legend, the reader is referred to the Web version of this article.)

mean wave direction and DWD produced using the ηuv data is plotted in Fig. 10. According to this figure, 85.7% of the difference was in the $\pm$ 15^o range, indicating that mostly two wave directions are very close to each other. However, the maximum difference is $-$ 102^o, which occurred at 10/27/00:00. The H_S measured by the GNSS buoy at this time was small (i.e., 0.43 m). The shapes of histogram obtained using the $en\eta$ and uvw data are very similar to that obtained from the ηuv data; 82.6% and 85.6% of the differences determined using the $en\eta$ and uvw data, respectively, were in the $\pm 15^o$ range. For brevity, these data are not shown herein.

3.6. Discussions on mean wave directions and directional wave spectrum

To clarify the reasons that the mean wave direction and directional wave spectrum obtained from the $en\eta$ at 10/26/00:00 considerably differed from those obtained using the ηuv and uvw data, the time-series data of displacements in both east and north directions obtained by the GNSS buoy at this time are plotted in Fig. 11. There are both low- and high-frequency oscillations during the 10-min measuring period. The high-frequency parts should be due to the ocean waves, whereas the low-frequency portions, with periods of approximately 90 s, may represent the infragravity waves, which have a typical period of 25–250 s (Munk, 1950). The capture of these low-frequency signals in the $en\eta$ GNSS solutions suggests that these data potentially have additional value for investigating infragravity waves. Because we are mainly interested in the ocean waves, in the data analysis, the signals with frequencies of >0.4 or <0.05 Hz are filtered out. However, the directional wave spectrum obtained after filtering out the signals in undesired frequency ranges was nearly the same as that obtained from the original signals. Thus, the extraordinarily low- and high-frequency movements did not lead to inaccurate directional wave parameters results.

Because the H_S at 10/26/00:00 was only 0.37 m, we examined the signal-to-noise ratio (SNR) of the items measured by the GNSS buoy. The SNR of the measured signals is defined as follows.

$$\mathrm{SNR} = \frac{\sigma_m}{\sigma_a} \tag{34}$$

where σ_m and σ_a indicate the standard deviation of measured signals and noise signals, respectively. σ_a specifies the accuracy of the measurements and their values for various measuring items are declared by the VBS-RTK positioning service used in this study. The values of σ_a for the displacements and velocities in the east, north, and upward directions measured by the GNSS buoy are also presented in Table 1. As shown in Table 1, the root-mean-square accuracies of the displacements and velocities are approximately 0.05 m and 0.017 m/s, respectively. Table 1 lists the SNRs of displacements ($en\eta$) and velocities (uvw) measured by

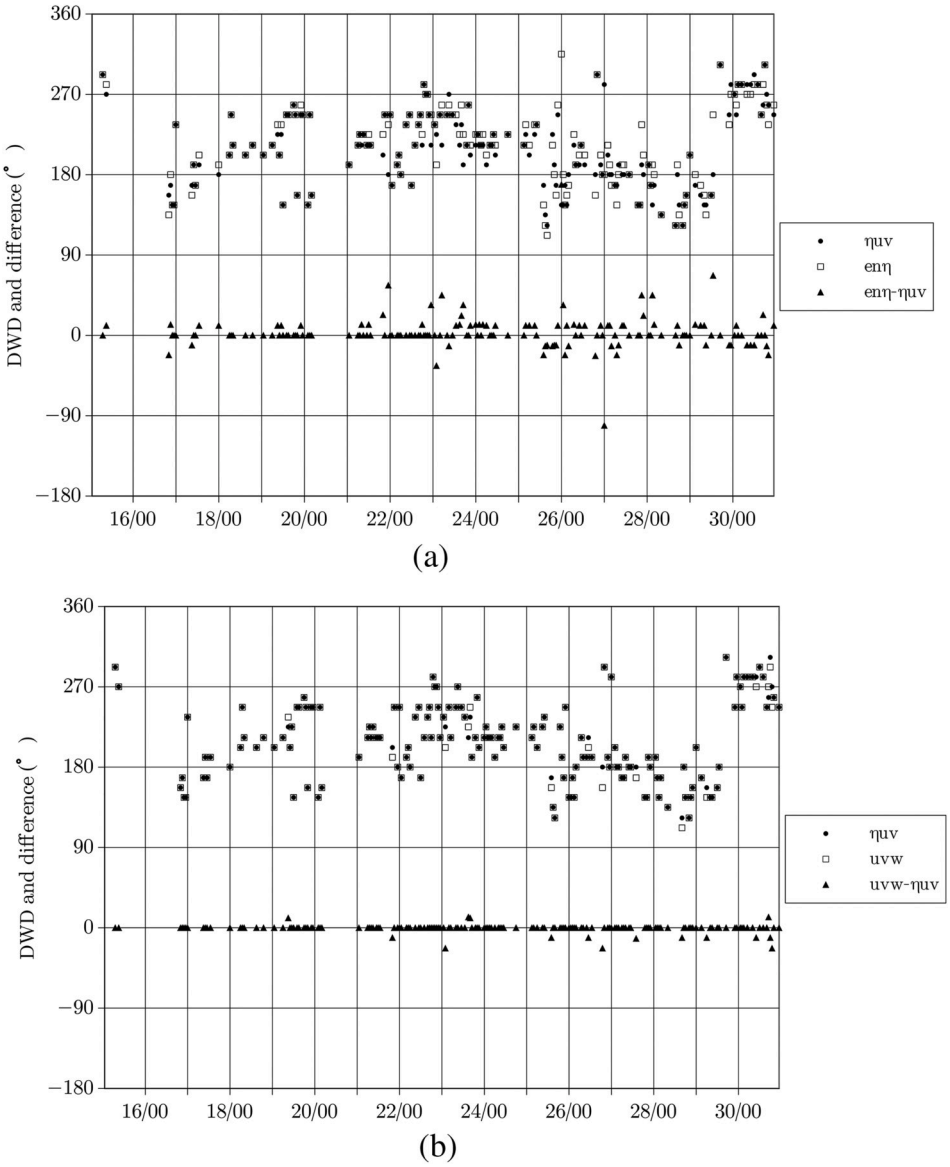

Fig. 9. Hourly time-series data of DWD and their differences obtained using (a) the *ηuv* and *enη* data and (b) the *ηuv* and *uvw* data, measured by the Small Liu-Qiu buoy. The field data were collected from 00:00 on October 15 to 23:00 on October 30 in 2016, but only hourly data with PGED = 1.0 were analyzed. The digits on the abscissa indicate the day and hour in October.

the GNSS buoy at 00:00 on October 26, 2016. Notably from Table 1 that the SNRs of displacements were approximately one order of magnitude smaller than those of velocities, indicating that the better method for determining the directional wave parameters should be using the *uvw* data, rather than the *enη* data.

Table 2 presents the mean and maximum absolute deviations of the mean wave direction obtained from the *enη* data. The deviation is determined by subtracting the mean wave direction obtained using the *enη* data from that obtained using the *uvw* data. The data analyzed here were collected from the field test from 10/15/00:00 to 10/30/23:00, 2016, with PGED = 1.00. The minimum SNR denotes the smallest SNR value among the samples. The number of samples corresponds to various H_S values. Notably, as shown in Table 2, the mean and maximum absolute deviations decreased considerably as the H_S increased. The mean absolute deviation was $.4.8^o$ when $H_S \geq 0.4\,m$. It reached $.12.0^o$ when $H_S < 0.4\,m$ and decreased to $.1.6^o$ when $H_S \geq 2.0\,m$. The maximum absolute deviation was 61^o when $H_S \geq 0.4\,m$. It reached 196° when $H_S < 0.4\,m$ and decreased to 4^o when $H_S \geq 2.0\,m$. Furthermore, when $H_S \geq 1.0\,m$, the mean wave directions obtained using the *enη* data were nearly identical to those obtained using the *uvw* data. Notably, the mean and maximum absolute deviations of the mean wave direction decreased as the minimum SNR of displacements increased, and the minimum SNR of displacements increased with the increase in the H_S.

Possible reasons why the small SNRs of the *enη* data tended to produce inaccurate directional wave parameters are the following: In this study, once the displacement and velocity data were obtained from the GNSS buoy, FFT was used to determine the cospectrum and quadrature spectrum for any pair of wave properties. The obtained cross-power spectra were then used to determine the Fourier coefficients of the DSF $D(f,\theta)$. Signals with small SNRs were contaminated with considerable noises. These noises produced inaccurate cross-power spectra, which led to inaccurate Fourier coefficients. This then generated errors

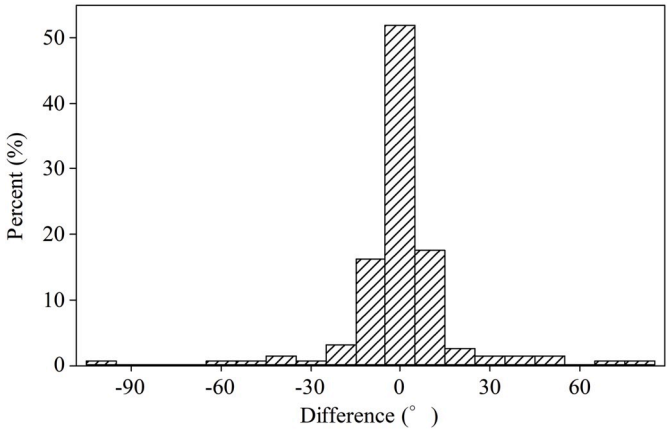

Fig. 10. Histogram of differences between the mean wave direction and DWD produced using the ηuv data.

in the directional wave parameters.

The mismatch in the directional wave parameters during low seas that we attributed to the poor performance of the $en\eta$ data was further confirmed by comparing the directional wave parameters obtained using the GNSS buoy data (either $en\eta$ or uvw) with the parameters obtained using the ATC sensor data. Under smooth sea conditions with $H_S < 0.4\ m$, a comparison of 37 hourly mean wave directions obtained from the GNSS buoy and ATC sensor data revealed that the mean error declined from $.9.5^o$ to $.2.1^o$ when uvw data were used instead of $en\eta$ data. The error was calculated by subtracting the value obtained using the ATC sensor data from that obtained using the GNSS buoy data. Similarly, the mean error of the DWD decreased from $.7.5^o$ to $-\ .4.9^o$ when uvw data were used instead of $en\eta$ data.

The results obtained in this study show that, when $H_S \geq 1.0\ m$, the directional wave parameters determined from any of the three GNSS data sets, namely $en\eta$, uvw, and ηuv, agreed well with each other. Therefore, any of these data sets is appropriate for determining the directional wave parameters under these ocean conditions. However, when $H_S < 1.0\ m$, the uvw and ηuv data are more appropriate than the $en\eta$ data for determining the directional wave parameters.

The aforementioned findings, as summarized in Conclusions 1 and 2, provide useful information for choosing appropriate GNSS data for determining directional wave parameters. Conclusion 3 suggests that examining the SNRs of the measured data under various sea states is a possible method of surveying intrinsic uncertainties in measured data used for determining directional wave parameters. These findings suggest also that wave-related observations, such as water surface elevation, pressure, acceleration, tilt, and velocity, can be combined to obtain directional wave parameters. However, for choosing appropriate data combination, intrinsic uncertainties in measured data must be examined.

3.7. Limitations using a GNSS buoy based on VBS-RTK positioning for ocean monitoring

As mentioned in Section 2.1, the data transmission between the GNSS receiver on the buoy and the VBS-RTK control center is conducted using a GPRS modem. The deployment range of the GNSS buoy is limited by network coverage because the GPRS modem requires a network signal for data transmission. The range, usually within a few kilometers, can be extended to a maximum distance of 20 km if PPK (post-processed kinematic) is used instead of the VBS-RTK positioning (Arroyo-Suarez et al., 2006). Nevertheless, PPK is not obtained in real time.

El-Mowafy et al. (2017) indicated that precise point positioning (PPP) technology can provide decimeter-level positioning accuracy by using a single receiver without a base station. Thus, PPP technology can be utilized anywhere. Several real-time, open-access commercial services are available for PPP positioning, such as IGS-RTS, the Trimble RTX service (Leandro et al., 2011), the Fugro G2 service (http://www.starfix.com/positioning-systems), and TERRASTAR (https://www.terr

Table 1
SNRs of $en\eta$ and uvw measured by the GNSS buoy at 00:00 on October 26, 2016.

Index	Displacements ($en\eta$)			Velocities (uvw)		
	east	north	upward	east	north	upward
σ_m	0.064 m	0.056 m	0.099 m	0.313 m/s	0.297 m/s	0.225 m/s
σ_a	0.02 m		0.05 m	0.017 m/s		
SNR	3.2	2.8	1.98	18.41	17.47	13.24

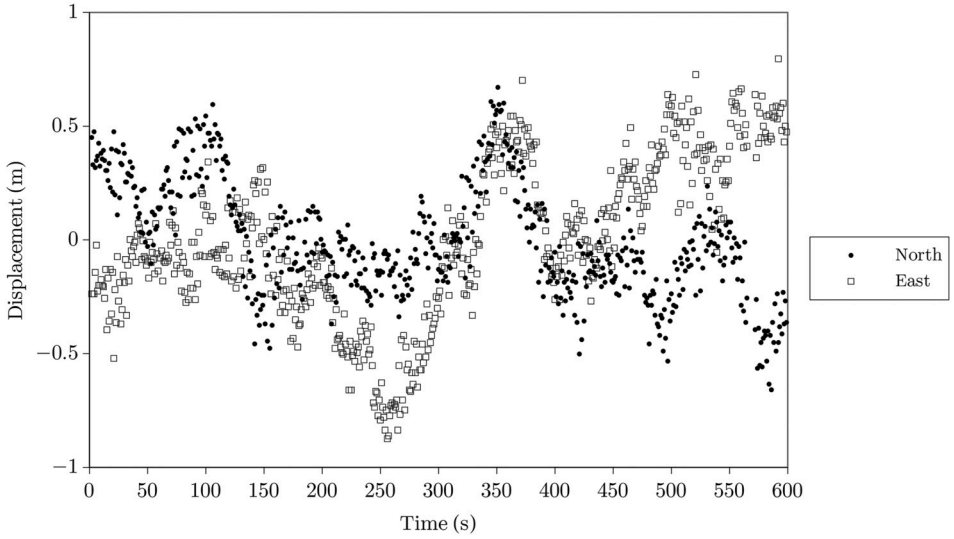

Fig. 11. Time-series data of horizontal displacements measured by the GNSS buoy at 00:00 on October 26, 2016; the measuring period lasted 10 min with a sampling rate of 1 Hz.

Table 2
Mean and maximum absolute deviations[a] of the mean wave direction obtained from the *enη* data.

Minimum SNR			Significant wave height (m) H_S	Number of samples	Mean absolute deviations (°)	Maximum absolute deviations (°)
east	north	upward				
1.93	2.31	1.40	$H_S < 0.4$	42	12.0	196
3.08	3.15	2.05	$H_S \geq 0.4$	118	4.8	61
9.06	7.45	5.17	$H_S \geq 1.0$	55	2.1	8
22.64	20.64	10.20	$H_S \geq 2.0$	18	1.6	4

[a] Subtracting the mean wave direction obtained using the *enη* data from that obtained using the *uvw* data.

astar.net). Therefore, the range limitation of the GNSS buoy can be alleviated if the global real-time PPP (RT PPP) service is used instead of VBS-RTK positioning. The accuracy of PPP technology can be improved to the centimeter level if satellite-based augmentation systems (SBAS) are implemented (Choy et al., 2017). Some commercial GNSS augmentation service providers, such as Novatel (with TerraStar-C corrections) (https://www.novatel.com/products/terrastar-gnss-corrections/#contentTab1), offer both horizontal and vertical centimeter-level positioning solutions for land and airborne applications.

In addition to the deployment range limitation, the GPRS connection dropout under severe weather conditions may influence the number of observed data with PGED = 1.0. In this case, a GNSS buoy provides less reliable ocean monitoring data compared with a conventional ATC sensor (Fig. 3). Moreover, as demonstrated in Sections 3.2 to 3.6, under smooth to slight sea conditions with $H_S < 1.0\ m$, only the *uvw* and *ηuv* GNSS data are recommended for use in determining the directional wave parameters.

4. Conclusions

This study applied the WFS method proposed by Longuet-Higgin et al. (1963) to investigate the variations in the directional wave parameters by utilizing three combinations of time-series data obtained by the GNSS buoy, such as *ηuv*, *enη*, and *uvw*. The data that analyzed in this study were collected from the field test by deploying the GNSS buoy developed by Lin et al. (2017a) in the Small Liu-Qiu waters, Taiwan. Only hourly data whose PGED = 1.0 are utilized to determine the directional wave parameters including the mean wave direction, directional spreading, directional wave spectrum, and dominant wave direction. Based on the present results, we may conclude the following.

1. In moderate and higher sea conditions, when $H_S \geq 1.0\ m$, the directional wave parameters determined from any of the three GNSS data sets, namely *enη*, *uvw*, and *ηuv*, agreed well with each other.
2. Under smooth to slight sea conditions with $H_S < 1.0\ m$, the *uvw* and *ηuv* data generate more accurate directional wave parameters than the *enη* data. Accordingly, when $H_S < 1.0\ m$, only the *uvw* and *ηuv* data are recommended for use for determining the directional wave parameters.
3. The less accurate directional wave parameters obtained from the *enη* data were associated with smaller SNR values of the displacement data (*enη*) compared with those of the velocity data (*uvw*). The SNR values of the *enη* data increased with H_S.
4. During the field tests, the maximum difference in the dominant wave direction and the maximum difference in the mean wave direction between the *enη* and *ηuv* data occurred at the same time, when the H_S was only 0.37 *m*.

Declaration of competing interest

The authors declare that they have no known competing financial interests or personal relationships that could have appeared to influence the work reported in this paper.

CRediT authorship contribution statement

Yen-Pin Lin: Methodology, Formal analysis, Writing - original draft. **Ching-Jer Huang:** Supervision, Writing - review & editing. **Sheng-Hsueh Chen:** Software.

Acknowledgment

The authors are grateful to the Central Weather Bureau (CWB) of Taiwan for providing the GNSS receiver and for allowing us to integrate the GNSS receiver into the Small Liu-Qiu buoy, which has been deployed for an operational monitoring of atmospheric and oceanographic data. This has made a real-time monitoring of 3D displacement and velocity from the GNSS buoy possible. The authors are also grateful to the anonymous reviewers for their helpful comments and suggestions.

References

Arroyo-Suarez, E.N., Mabey, D.L., Hsiao, V., Phillips, R., 2006. GPS buoys nautical measurements. GPS World 17 (5), 46–50.
Benoit, M., 1992. Practical comparative performance survey of methods used for estimating directional wave spectra from heave-pitch-roll data. In: Proceedings of the 23rd Int. Conf. on Coastal Eng., pp. 62–75. October 4-9, Venice, Italy.
Benoit, M., Teisson, C., 1994. Laboratory comparison of directional wave measurement systems and analysis techniques. In: Proceedings of the 24th Int. Conf. on Coastal Eng., pp. 42–56 (Kobe, Japan).
Choy, S., Kuckartz, J., Dempster, A.G., Rizos, C., 2017. GNSS satellite-based augmentation systems for Australia. GPS Solut. 21, 835–848. https://doi.org/10.1007/s10291-016-0569-2.
Doong, D.J., Lee, B.C., Kao, C.C., 2011. Wave measurements using GPS velocity signals. Sensors 11, 1043–1058.
Earle, M.D., 1996. Nondirectional and Directional Wave Data Analysis Procedures. National Data Buoy Center, National Oceanic and Atmospheric Administration, U.S. Department of Commerce: Stennis Space Center, USA.
El-Mowafy, A., Deo, M., Kubo, N., 2017. Maintaining real-time precise point positioning during outages of orbit and clock corrections. GPS Solut. 21, 937–947.
EurOtop, 2018. Manual on wave overtopping of sea defences and related structures. In: Van der Meer, J.W., Allsop, N.W.H., Bruce, T., De Rouck, J., Kortenhaus, A., Pullen, T., Schüttrumpf, H., Troch, P., Zanuttigh, B. (Eds.), An Overtopping Manual Largely Based on European Research, but for Worldwide Application. www.overtopping-manual.com.
Goda, Y., 2000. Random Seas and Design of Maritime Structures, second ed. World Scientific, Singapore. ISBN 981-02-3256-X.
Harigae, M., Yamaguchi, I., Kasai, T., Igawa, H., Nakanishi, H., Murayama, T., Iwanaka, Y., Suko, H., 2005. Abreast of the waves: open-sea sensor to measure height and direction. GPS World 16, 16–26.
Hashimoto, N., Konbune, K., 1988. Directional spectrum estimation from a Bayesian approach. In: Coast. Eng. Proc., 1, pp. 62–76.
He, K., 2015. GNSS Kinematic Position and Velocity Determination for Airborne Gravimetry. Technische Universitaet Berlin (Germany), Potsdam, Germany. ISSN 2190-7110.
Kaplan, E.D., Hegarty, C.J. (Eds.), 2017. Understanding GPS/GNSS: Principles and Applications, third ed. Artech House.
Kuik, A.J., Van Vledder, G.P.H., Holthuijsen, L.H., 1988. A method for the routine analysis of pitch-and-roll buoy wave data. J. Phys. Oceanogr. 18 (7), 1020–1034.
Leandro, R., Landau, H., Nitschke, M., Glocker, M., Seeger, S., Chen, X., Deking, A., BenTahar, M., Zhang, F., Ferguson, K., Stolz, R., Talbot, N., Lu, G., Allison, T., Brandl, M., Gomez, V., Cao, W., Adrian Kipka, A., 2011. RTX positioning: the next generation of cm-accurate real-time GNSS positioning. In: Proc ION GNSS 2011. Institute of Navigation, Portland, pp. 1460–1475.
Lin, Y.P., Huang, C.J., Chen, S.H., Doong, D.J., Kao, C.C., 2017a. Development of a GNSS buoy for monitoring water surface elevations in estuaries and coastal areas. Sensors 17, 172. https://doi.org/10.3390/s17010172.
Lin, Y.P., Huang, C.J., Doong, D.J., Kao, C.C., 2017b. Performance of the GNSS buoy for monitoring tides and ocean waves in coastal areas. J. Coast. Ocean Eng. 17 (3), 175–196 (Chinese).

Lin, Y.P., 2018. Development and applications of a GNSS buoy for monitoring tides and ocean waves in coastal areas. In: Dissertation for Doctor of Philosophy in Hydraulic and Ocean Engineering, National Cheng Kung University, Tainan, Taiwan, p. 82.
Longuet-Higgins, M.S., Cartwright, D.E., Smith, N.D., 1963. Observations of the directional spectrum of sea waves using the motions of a floating buoy. In: Ocean Wave Spectra, Proc. Conf., Easton, Maryland, May 1-4, 1961. Prentice Hall, pp. 111–136.
McConnell, K.J., 1998. Revetment Systems against Wave Attack: a Design Manual. Thomas Telford, London. ISBN 0-7277-2706-0.
Munk, W., 1950. Origin and generation of waves. In: Proceedings of First Conference on Coastal Engineering, Long Beach, California, pp. 1–4.
Panahi, R., Ghasemi, K.A., Shafieefar, M., 2015. Development of a bi-modal directional wave spectrum. Ocean Eng. 105, 104–111.
Pedersen, T., Siegel, E., 2008. Wave measurements from subsurface buoys. In: Proceedings of the IEEE/OES/CMTC 9th Working Conference on Current Measurement Technology, pp. 224–233.
Riedel, J.S., Healey, A.J., 2005. Estimation of Directional Wave Spectra from an Autonomous Underwater Vehicle. Naval Postgraduate School, Center for Autonomous Underwater Vehicle Research, Monterey, CA, p. 10.
Sickel, J.V., 2015. GPS for Land Surveyors, fourth ed. CRC press.
Topcon Positioning Systems, Inc, 2012. MR-1 Receiver Reference Guide. Rev A, Topcon Positioning Systems, Inc., Livermore, CA, USA.
Work, P.A., 2008. Nearshore directional wave measurements by surface-following buoy and acoustic Doppler current profiler. Ocean Eng. 35 (8–9), 727–737.
Wu, C.T., Hsiao, C.Y., Hsieh, P.S., 2013. Using UAV and VBS-RTK for rapid reconstruction of environmental 3D elevation data of the Typhoon Morakot disaster area and disaster scale assessment. J. Chin. Soil Water Conserv. 44, 23–33.
Young, I.R., 1994. On the measurement of directional wave spectra. Appl. Ocean Res. 16 (5), 283–294.